

# Cross frequency coupling in next generation inhibitory neural mass models

Cite as: Chaos **30**, 053121 (2020); <https://doi.org/10.1063/1.5125216>

Submitted: 21 August 2019 . Accepted: 22 April 2020 . Published Online: 11 May 2020

Andrea Ceni, Simona Olmi , Alessandro Torcini , and David Angulo-Garcia 



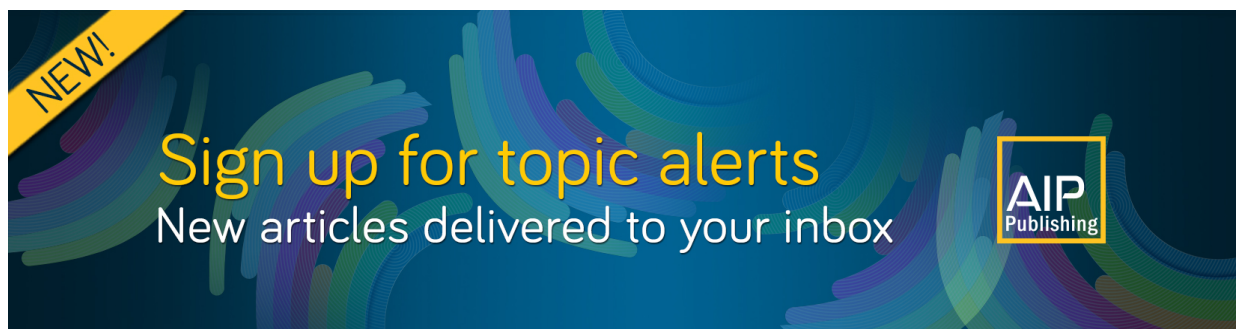
View Online



Export Citation



CrossMark



**NEW!**  
Sign up for topic alerts  
New articles delivered to your inbox  
AIP  
Publishing



# Cross frequency coupling in next generation inhibitory neural mass models

Cite as: Chaos 30, 053121 (2020); doi: 10.1063/1.5125216

Submitted: 21 August 2019 · Accepted: 22 April 2020 ·

Published Online: 11 May 2020



View Online



Export Citation



CrossMark

Andrea Ceni,<sup>1</sup> Simona Olmi,<sup>2,3,4,a)</sup>  Alessandro Torcini,<sup>5,3</sup>  and David Angulo-Garcia<sup>6</sup> 

## AFFILIATIONS

<sup>1</sup>Department of Computer Science, College of Engineering, Mathematics and Physical Sciences, University of Exeter, Exeter EX4 4QF, United Kingdom

<sup>2</sup>Inria Sophia Antipolis Méditerranée Research Centre, 2004 Route des Lucioles, 06902 Valbonne, France

<sup>3</sup>CNR—Consiglio Nazionale delle Ricerche—Istituto dei Sistemi Complessi, via Madonna del Piano 10, 50019 Sesto Fiorentino, Italy

<sup>4</sup>INFN, sez. Firenze, 50019 Sesto Fiorentino, Italy

<sup>5</sup>Laboratoire de Physique Théorique et Modélisation, Université de Cergy-Pontoise, CNRS, UMR 8089, 95302 Cergy-Pontoise cedex, France

<sup>6</sup>Grupo de Modelado Computacional—Dinámica y Complejidad de Sistemas, Instituto de Matemáticas Aplicadas, Universidad de Cartagena, Carrera 6 #36-100, 130001 Cartagena de Indias, Colombia

<sup>a)</sup>Author to whom correspondence should be addressed: [simona.olmi@cnr.it](mailto:simona.olmi@cnr.it)

## ABSTRACT

Coupling among neural rhythms is one of the most important mechanisms at the basis of cognitive processes in the brain. In this study, we consider a neural mass model, rigorously obtained from the microscopic dynamics of an inhibitory spiking network with exponential synapses, able to autonomously generate collective oscillations (COs). These oscillations emerge via a super-critical Hopf bifurcation, and their frequencies are controlled by the synaptic time scale, the synaptic coupling, and the excitability of the neural population. Furthermore, we show that two inhibitory populations in a master–slave configuration with different synaptic time scales can display various collective dynamical regimes: damped oscillations toward a stable focus, periodic and quasi-periodic oscillations, and chaos. Finally, when bidirectionally coupled, the two inhibitory populations can exhibit different types of  $\theta$ – $\gamma$  cross-frequency couplings (CFCs): phase-phase and phase-amplitude CFC. The coupling between  $\theta$  and  $\gamma$  COs is enhanced in the presence of an external  $\theta$  forcing, reminiscent of the type of modulation induced in hippocampal and cortex circuits via optogenetic drive.

Published under license by AIP Publishing. <https://doi.org/10.1063/1.5125216>

Under healthy conditions, the brain's activity consists of a series of intermingled oscillations, generated by large ensembles of neurons, which provide a functional substrate for information processing. Understanding how single neuron properties influence neuronal population dynamics could help in the comprehension of the collective behaviors emerging during cognitive processes. Here, we consider a neural mass model, which reproduces exactly the macroscopic activity of a network of spiking Quadratic Integrate-and-Fire (QIF) neurons. This mean-field model is employed to shed some light on an important and pervasive neural mechanism underlying information processing in the brain: the  $\theta$ – $\gamma$  cross-frequency coupling. In particular, we will explore in detail the conditions under which two coupled inhibitory neural populations, characterized by slow and fast synaptic kinetics, can generate these functionally relevant coupled rhythms.

## I. INTRODUCTION

Neural rhythms represent the fundamental elements of information coding in the brain.<sup>16</sup> These rhythms emerge due to the activity of large populations of neurons that orchestrate their firing in partially synchronous bursts and selectively communicate with other populations, producing complex functional interactions.<sup>18,60</sup>

One of the most prominent rhythmic interactions appearing in the brain is the  $\theta$ – $\gamma$  coupling, exhibited between the slow oscillating  $\theta$  band (4–12 Hz) and the faster  $\gamma$  rhythm (25–100 Hz).<sup>40</sup> This specific frequency interaction is an example of a more general mechanism termed Cross-Frequency-Coupling (CFC).<sup>18,34</sup> CFC has been proposed to be at the basis of sequence representation, long distance communication, sensory parsing, and de-multiplexing.<sup>31,34</sup> CFC can manifest in a variety of ways depending on the type of modulation that one rhythm imposes on the other (amplitude–amplitude,

amplitude–frequency, phase–amplitude, frequency–frequency, frequency–phase, or phase–phase).<sup>34</sup>

In this article, we will mainly focus on Phase–Phase (P–P) coupling of  $\theta$  and  $\gamma$  rhythms, with some analysis also of Phase–Amplitude (P–A) coupling. In particular, P–P coupling refers to  $n:m$  phase locking between  $\gamma$  and  $\theta$  phase oscillations.<sup>54</sup> This rhythmic interaction has been demonstrated to play a role in visual tasks in humans<sup>30</sup> and it has been identified in the rodent hippocampus during maze exploration.<sup>8</sup> The P–A coupling (or  $\theta$ -nested  $\gamma$  oscillations) denotes the fact that the phase of the theta-oscillation modifies the amplitude of the gamma waves. P–A coupling has been shown to support the formation of new episodic memories in the human hippocampus<sup>39</sup> and to emerge in various parts of the rodent brain during optogenetic theta stimulations *in vitro*.<sup>3,13,14,50</sup>

Phase–amplitude  $\theta$ – $\gamma$  CFC is believed to serve as a mechanism to transfer information from large-scale brain networks, operating at low-frequency, to fast timescale, associated with local cortical circuits.<sup>18</sup> In this context, it has been reported that P–A CFC can emerge in the primary visual cortex of anesthetized macaques under naturalistic visual stimuli. These experimental results have been well reproduced by considering sparsely connected excitatory–inhibitory networks under external forcing.<sup>45,46</sup> However, on a general ground, it is still unclear if  $\gamma$  rhythms in the brain arise due to pyramidal–interneuron circuits (PING mechanism) or to purely inhibitory networks (ING mechanism).<sup>18</sup> In particular, recent optogenetics studies on the rodent hippocampus *in vitro* demonstrate that ING<sup>50</sup> or PING<sup>14</sup> mechanisms can be both at the basis of  $\gamma$  oscillations. Furthermore, there are also indications that  $\theta$  activity can be generated by multiple local circuits<sup>7</sup> and it can be regulated by inhibitory networks.<sup>62</sup>

In a seminal work, White *et al.*<sup>61</sup> have shown that two inhibitory neural populations with fast and slow  $GABA_A$  kinetics<sup>1</sup> can provide a substrate for  $\theta$ – $\gamma$  rhythms. The model was inspired by a series of experimental evidence: first, distinct populations of interneurons in the hippocampus generate inhibitory post-synaptic potentials (IPSPs) mediated via  $GABA_{A,fast}$  or  $GABA_{A,slow}$  receptors;<sup>5</sup> second, the existence of projections from  $GABA_{A,slow}$  to  $GABA_{A,fast}$  cells.<sup>6</sup>

In an attempt to understand the complex interactions emerging during CFC, several mathematical models describing the activity of a large ensemble of neurons have been proposed.<sup>22</sup> Widely known examples include the phenomenologically based Wilson–Cowan<sup>63</sup> and Jansen–Rit<sup>33</sup> neural mass models. While the usefulness of these heuristic models has been demonstrated in a variety of applications, they are not related to any underlying microscopic dynamics of a neuronal population. Furthermore, these models are expected to provide appropriate levels of description for many thousands of near identical interconnected neurons with a preference to operate in synchrony.<sup>21</sup>

Recently, the Ott–Antonsen ansatz has allowed us to exactly obtain the macroscopic evolution of phase oscillator networks, fully coupled via a purely sinusoidal field.<sup>49</sup> It is possible to transfer this approach to ensembles of pulse-coupled Quadratic Integrate-and-Fire (QIF) neurons and, therefore, to derive in an exact manner, a macroscopic description for these neural populations.<sup>21,43,47,51</sup> The QIF neuronal model is particularly relevant, since it can be related by a change of variable, to the  $\theta$ -neuron, which represents the normal form of Hodgkin’s class I excitable membranes. Therefore, the

QIF neuron is expected to describe the dynamics of all class I neurons in proximity to the saddle-node on a limit cycle bifurcation.<sup>27</sup> In particular, in Ref. 47, the authors have been able to derive, for a network of fully coupled QIF neurons with instantaneous synapses, an exact neural mass model in terms of the population firing rate and the average membrane potential. This reduced model allows us to describe, exactly, the dynamics of a microscopic heterogeneous population in terms of macroscopic variables for any level of synchronization among the neurons, at variance with usual neural mass models.<sup>21,47</sup>

In this paper, inspired by the work of White *et al.*,<sup>61</sup> we will employ the exact neural mass model derived by Devalle *et al.*<sup>24</sup> for one population of globally coupled QIF neurons with exponential synapses to study the emergence of mixed  $\theta$ – $\gamma$  oscillations in coupled inhibitory populations with fast and slow synaptic kinetics. In particular, in Subsection III A, we will characterize the dynamical behavior of a single population and review the conditions required to observe collective oscillations (COs). Afterward, in Subsection III B, we will analyze the response of the population to an external sinusoidal forcing paying special attention to the emergence of phase synchronization. We will then consider in Subsection III C the possible macroscopic dynamics displayed by two coupled inhibitory populations characterized by different synaptic time scales in a master–slave configuration, where the slow population drives the fast one. Finally, Subsection III D is focused on the study of the emergence of  $\theta$ – $\gamma$  CFCs among the COs displayed by the two bidirectionally coupled populations.

## II. MODEL AND METHODS

### A. Network dynamics

Throughout this paper, we will examine either one or two populations of QIF neurons interacting via inhibitory post-synaptic potentials (IPSPs) with an exponential profile. In this framework, the activity of the population  $l \in \{A, B\}$  is described by the dynamics of the membrane potentials  $V_i^{(l)}$  of its neurons and of the associated synaptic fields  $S_i^{(l)}$ . Here, we will assume a fully coupled topology for all networks, hence each neuron within a certain population is subject to the same synaptic field  $S^{(l)}$ , where the neuron index has been dropped. Therefore, the dynamics of the network can be written as

$$\begin{aligned} \tau \dot{V}_i^{(l)} &= (V_i^{(l)})^2 + \eta_i^{(l)} + J_{ll} \tau S^{(l)} + J_{lk} \tau S^{(k)} + I^{(l)}(t), \\ \tau_d^{(l)} \dot{S}^{(l)} &= -S^{(l)} + \frac{1}{N^{(l)}} \sum_{t_j^{(l)}} \delta(t - t_j^{(l)}), \\ i &= 1, \dots, N^{(l)}, \quad l, k \in \{A, B\}, \end{aligned} \quad (1)$$

where  $\tau = 10$  ms is the membrane time constant which is assumed equal for both populations,  $\eta_i^{(l)}$  is the excitability of the  $i$ th neuron of population  $l$ ,  $J_{lk}$  is the strength of the inhibitory synaptic coupling of population  $l$  acting on population  $k$ , and  $I^{(l)}(t)$  is a time dependent external current applied on population  $l$ . The synaptic field  $S^{(l)}(t)$  is the linear super-position of the all exponential IPSPs  $s(t) = e^{-t/\tau_d^{(l)}}$  emitted within the  $l$  population in the past. Due to the quadratic term in the membrane potential evolution, which allows

the variable to reach infinity in a finite time, the emission of the  $j$ th spike in the network occurs at time  $t_j^{(l)}$  whenever  $V_i^{(l)}(t_j^{(l)-}) \rightarrow +\infty$ , while the reset mechanism is modeled by setting  $V_i^{(l)}(t_j^{(l)+}) \rightarrow -\infty$ , immediately after the spike emission.

For reasons that will be clear in the next paragraph, we will also assume that the neuron excitability values  $\eta_i^{(l)}$  are randomly distributed according to a Lorentzian probability density function (PDF)

$$g(\eta) = \frac{1}{\pi} \frac{\Delta^{(l)}}{(\eta - \bar{\eta}^{(l)})^2 + (\Delta^{(l)})^2}, \quad (2)$$

where  $\bar{\eta}^{(l)}$  is the median and  $\Delta^{(l)}$  is the half-width half-maximum (HWHM) of the PDF. For simplicity, we set  $\bar{\eta} = 1$  throughout the paper, unless otherwise stated.

In order to characterize the macroscopic dynamics, we will employ the following indicators:

$$r^{(l)}(t) = \frac{1}{N^{(l)}\Delta t} \sum_{t_j^{(l)}} \delta(t - t_j^{(l)}), \quad v^{(l)}(t) = \frac{1}{N^{(l)}} \sum_j^{N^{(l)}} V_j^{(l)}(t),$$

which represent the average population activity of each network and the average membrane potential, respectively. In particular, the average population activity of the  $l$ -network  $r^{(l)}(t)$  is given by the number of spikes emitted in a time unit  $\Delta t$ , divided by the total number of neurons. Furthermore, the emergence of COs in the dynamical evolution, corresponding to periodic motions of  $r^{(l)}(t)$  and  $v^{(l)}(t)$ , will be characterized in terms of their frequencies  $\nu^{(l)}$ .

### B. Mean-field evolution

In the limit of infinitely many neurons  $N^{(l)} \rightarrow \infty$  we can derive, for each population  $l$ , the evolution of the PDF  $\rho^{(l)}(V|\eta, t)$  describing the probability distribution of finding a neuron with potential  $V$  and excitability  $\eta$  at a time  $t$  via the continuity equation

$$\frac{\partial \rho^{(l)}(V|\eta, t)}{\partial t} = - \frac{\partial \mathcal{F}^{(l)}(V|\eta, t)}{\partial V^{(l)}}, \quad (3)$$

$$\mathcal{F}^{(l)}(V|\eta, t) = \rho^{(l)} \left( \frac{(V^{(l)})^2 + \eta^{(l)} + \mathcal{I}^{(l)}}{\tau} \right),$$

where  $\mathcal{F}^{(l)}(V|\eta, t)$  is the probability flux, while  $\mathcal{I}^{(l)} = J_{ll}\tau S^{(l)} + J_{kl}\tau S^{(k)} + I^{(l)}(t)$  (for  $l, k \in \{A, B\}$ ) is the contribution of all synaptic currents plus the external input. The continuity equation (3) is completed with the boundary conditions describing the firing and reset mechanisms of the network model (1), which reads as

$$\lim_{V \rightarrow -\infty} \mathcal{F}^{(l)}(V|\eta, t) = \lim_{V \rightarrow \infty} \mathcal{F}^{(l)}(V|\eta, t). \quad (4)$$

Following the theoretical framework developed by Montbrío *et al.*,<sup>47</sup> one can apply the Ott-Antonsen ansatz<sup>49</sup> to obtain an exact macroscopic description of the infinite-dimensional 2-population system (1) in terms of collective variables. In order to obtain exact analytic results it is crucial to assume that the distribution of the neuronal excitabilities is a Lorentzian PDF. In the case of the QIF model, the macroscopic variables for each  $l$ -population are the instantaneous

firing rate  $r^{(l)}$ , the average membrane potential  $v^{(l)}$ , and the mean synaptic activity  $s^{(l)}$ , which evolve according to the following:

$$\begin{aligned} \dot{r}^{(l)} &= \frac{\Delta^{(l)}}{\tau^2\pi} + \frac{2r^{(l)}v^{(l)}}{\tau}, \\ \dot{v}^{(l)} &= \frac{(v^{(l)})^2 + \bar{\eta}^{(l)} + I^{(l)}(t)}{\tau} + J_{ll}s^{(l)} + J_{kl}s^{(k)} - \tau(\pi r^{(l)})^2, \\ \dot{s}^{(l)} &= \frac{1}{\tau_d^{(l)}} [-s^{(l)} + r^{(l)}] \end{aligned} \quad (5)$$

for  $l, k \in \{A, B\}$ .

As shown by Montbrío *et al.*,<sup>47</sup> the reported approach can be extended to Gaussian or uniform distributions of the excitabilities; for all these distributions, the observed dynamical regimes are essentially the same as for the Lorentzian distribution.

### C. Dynamical indicators

We make use of two dynamical indicators to characterize the evolution of the mean-field (MF) model (5): a Poincaré section and the corresponding Lyapunov Spectrum (LS).

The considered Poincaré section is defined as the manifold  $\dot{r}^{(A)}(\bar{t}) = 0$  with  $\dot{r}^{(A)}(\bar{t}^-) > 0$ , which amounts to identify the local maxima  $r_{max}$  of the time trace  $r^{(A)}(t)$ . On the other hand, to compute the LS, one should consider the time evolution of the tangent vector  $\delta = \{\delta r^{(A)}, \delta v^{(A)}, \delta s^{(A)}, \delta r^{(B)}, \delta v^{(B)}, \delta s^{(B)}\}$ , resulting from the linearization of the original system Eq. (5), namely,

$$\begin{aligned} \delta \dot{r}^{(l)} &= \frac{2(r^{(l)}\delta v^{(l)} + v^{(l)}\delta r^{(l)})}{\tau}, \\ \delta \dot{v}^{(l)} &= \frac{2v^{(l)}\delta v^{(l)}}{\tau} + J_{ll}\delta s^{(l)} + J_{kl}\delta s^{(k)} - 2\pi^2\tau r^{(l)}\delta r^{(l)}, \\ \delta \dot{s}^{(l)} &= \frac{-\delta s^{(l)} + \delta r^{(l)}}{\tau_d^{(l)}} \end{aligned} \quad (6)$$

for  $l, k \in \{A, B\}$ .

The LS is thus composed of six Lyapunov Exponents (LEs)  $\{\lambda_i\}$  (three LEs in the case of one population), which quantify the average growth rates of infinitesimal perturbations along the different orthogonal manifolds estimated as

$$\lambda_i = \lim_{t \rightarrow \infty} \frac{1}{t} \log \frac{|\delta(t)|}{|\delta_0|}, \quad (7)$$

by employing the well known technique described in Benettin *et al.*<sup>9</sup> to maintain the tangent vectors ortho-normal during the evolution. In particular, in a dissipative system, one has a fixed point whenever the maximal Lyapunov is negative, a periodic motion if  $\lambda_1 = 0$  and  $\lambda_2 < 0$ , a quasi-periodic motion on a Torus  $T^N$  if  $\lambda_1 = \lambda_2 = \dots = \lambda_N = 0$ , and a chaotic motion if the maximal Lyapunov is positive.<sup>2,48</sup>

From the knowledge of the LS, one can obtain an estimation of the fractal dimension of the corresponding invariant set in terms of the so-called Kaplan–Yorke dimension  $D_{KY}$ ,<sup>35</sup> defined implicitly as

$$\sum_{i=1}^{D_{KY}} \lambda_i \equiv 0. \quad (8)$$



From this definition, a simple linear interpolation gives the following explicit expression:

$$D_{KY} = k + \frac{\sum_{i=1}^k \lambda_i}{|\lambda_{k+1}|}, \quad (9)$$

where  $k$  is the maximal value for which the sum of the first  $k$  Lyapunov exponents is still positive (for more details, see Ref. 48).

#### D. Locking characterization

To investigate the capability of two interacting populations to lock their dynamics in a biologically relevant manner, we measure the degree of phase synchronization in the reduced system (5). Therefore, we extract the phase of the population activity by performing the Hilbert transform  $\mathcal{H}[\cdot]$  of the firing rate for each population  $l \in \{A, B\}$ , thus obtaining the imaginary part of the analytic signal: namely,  $\phi^{(l)}(t) := r^{(l)}(t) + j\mathcal{H}[r^{(l)}(t)]$ . The evolution of the phase in time is then obtained as  $\Phi^{(l)}(t) = \arg[\phi^{(l)}(t)]$ . A generalized phase difference of the  $n : m$  phase-locked mode can be defined as

$$\Delta\Phi_{nm}(t) = n\Phi^{(A)} - m\Phi^{(B)}, \quad (10)$$

and the degree of synchronization in the phase locked regime can be quantified in terms of the Kuramoto order parameter for the phase difference, namely,

$$\rho_{nm} = |\langle e^{j\Delta\Phi_{nm}(t)} \rangle|, \quad (11)$$

where  $\langle \cdot \rangle$  denotes a time average, and  $|\cdot|$  is the norm of the complex number.<sup>8,36</sup>

### III. RESULTS

#### A. Self sustained oscillations in one population

First, by following the procedure outlined by Devalle *et al.*,<sup>24</sup> we analyze the case of a single population with self-inhibition in the absence of any external drive. Without lack of generality, we take into account just population A: this amounts to a set of only three equations in (5) with  $J_{BA} = J^{(A)}(t) = 0$ . For simplicity in the notation, we finally drop the indices denoting the populations.

In the fully coupled QIF network, oscillations can be observed only for IPSPs of finite duration—namely, exponential in the present case. In particular, COs appear when the equilibrium point of the macroscopic system  $(r_0, v_0, s_0)$  undergoes a Hopf bifurcation. Simulations of the QIF network model and the corresponding MF dynamics are compared in Fig. 1, revealing a very good agreement both in the asynchronous and in the oscillatory state. In particular, for the parameters considered in Fig. 1, the super-critical Hopf bifurcation takes place at  $\tau_d^{(H)} = 4.95$  ms and Figs. 1(a)–1(c) refer to a stable focus for the MF at  $\tau_d < \tau_d^{(H)}$ , while Figs. 1(d) and 1(e) to a stable limit cycle for  $\tau_d > \tau_d^{(H)}$ .

Due to the simplicity of the reduced model, it is also possible to parametrize the Hopf boundaries, where the asynchronous state loses stability as a function of the marginally stable solution

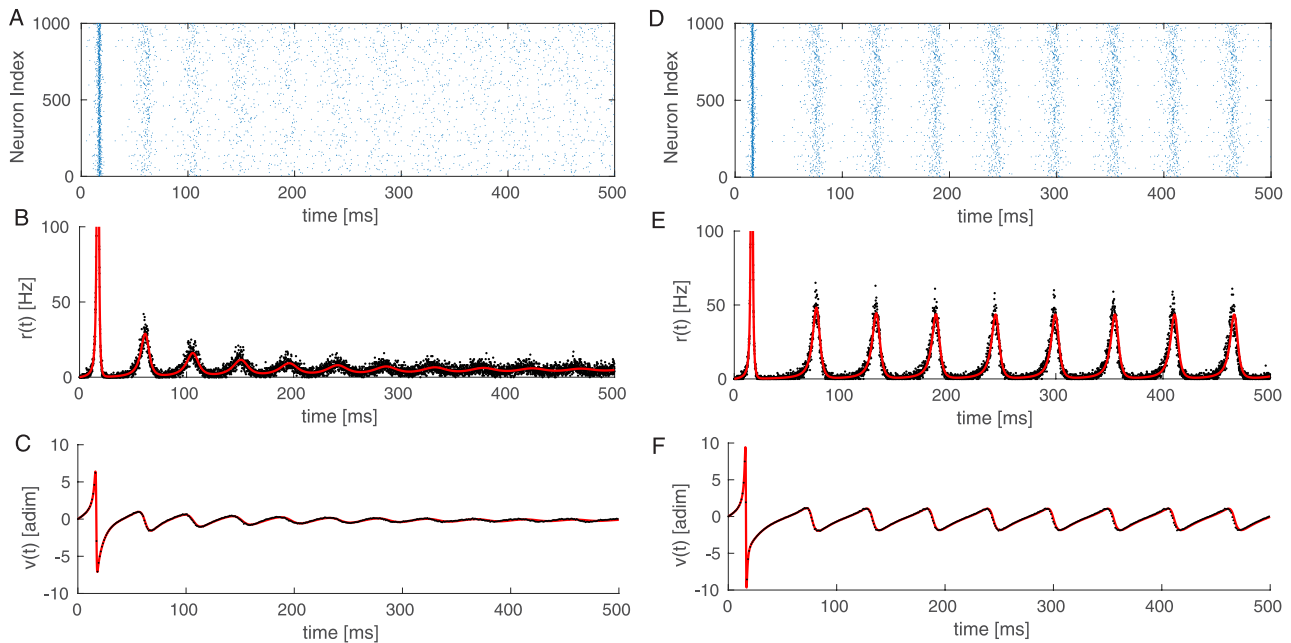


**FIG. 1.** Oscillations in a self-inhibited QIF population: Left and right columns refer to damped and self-sustained COs, respectively. From top to bottom: raster plots (a) and (d); instantaneous firing rate  $r(t)$  (b) and (e); and average membrane potential  $v(t)$  (c) and (f). The network simulations are reported as black dots, while the mean-field dynamics (5) is shown as a red line. For the network simulation,  $N = 10\,000$  QIF units are simulated. Left and right panels were obtained with  $\tau_d = 3$  ms and  $\tau_d = 8$  ms, respectively. Other parameters:  $\bar{\eta} = 1$ ,  $\Delta = 0.05$ ,  $J = -20$ , and  $\tau = 10$  ms.

$(r_0, v_0, s_0)$ . In particular, taking  $\tau_d$  and  $J$  as bifurcation parameters, one can verify that the boundaries of the Hopf bifurcation curves are defined by the following:

$$\tau_d^{(H)} = \frac{9\tau v_0^2 \bar{\eta} \tau - \pi^2 r_0^2 \tau^3 \pm \tau \sqrt{(\bar{\eta} - \pi^2 r_0^2 \tau^2)^2 + 2v_0^2 (9\bar{\eta} - 41\pi^2 r_0^2 \tau^2) + 17v_0^4}}{16 (\pi^2 r_0^2 \tau^2 v_0 + v_0^3)}, \tag{12}$$

$$J^{(H)} = \frac{\bar{\eta} + v_0^2}{r_0 \tau} - \pi^2 r_0 \tau. \tag{13}$$

The equilibrium values are related by the equalities  $v_0 = -\Delta/(2\tau\pi r_0)$  and  $s_0 = r_0$ , with  $r_0$  acting as a free parameter (see the Appendix for more details).

The phase diagrams showing the existence of self sustained oscillations in the  $\{r_0, \tau_d\}$  plane are displayed in Fig. 2(a), for three values of  $\Delta$ : the region inside the closed curves corresponds to the oscillating regime. Upon decreasing the dispersion of the excitability ( $\Delta$ ), the region of oscillatory behavior increases. This result highlights that some degree of homogeneity in the neural population is required in order to sustain a collective activity. In particular, for dispersions larger than a critical value  $\Delta_c$ , it is impossible for the system to sustain COs (for the parameter employed in the figure,  $\Delta_c \approx 0.1453$ ).

The inset in Fig. 2(a) displays the same boundaries in the  $\{\tau_d, J\}$  plane. From this figure, one can observe that the ranges of inhibitory strengths and of synaptic times required to sustain oscillations are negatively correlated with  $\Delta$ : upon increasing (decreasing)  $\Delta$ , the range of inhibitory strength and of synaptic times required to sustain oscillations decreases (increases). Thus indicating that the more heterogeneous the system, the more the parameters  $J$  and  $\tau_d$  should be finely tuned in order to have COs. It is worth mentioning that for

instantaneous synapses (corresponding to  $\tau_d \rightarrow 0$ ), no oscillations can emerge autonomously in fully coupled systems with homogeneous synaptic coupling as shown by Devalle *et al.*<sup>24</sup> and in Fig. 2. However, COs can be observed in sparse balanced networks with instantaneous synapses and in the absence of any delay in the signal transmission.<sup>25</sup>

In order to understand the role played by the different parameters in modifying the frequency of the COs, we have estimated this frequency for  $\Delta = 0.01$  in the  $(\tau_d, J)$ -plane. The results are shown as a heat-map in Fig. 2(b). It turns out that the frequency decreases for increasing values of  $\tau_d$  and of  $|J|$  and that frequencies in the  $\gamma$  range are observable only for  $\tau_d \leq 10$  ms and  $J > -20$ .

It is also worth noticing the fundamental role played by the self-inhibition in sustaining the autonomously generated oscillations, as it becomes clear from Eq. (12), since the Hopf bifurcations exist only for negative values of  $J$ .

From these results, we can conclude that a single population of QIF neurons can self sustain oscillations with a wide range of frequencies  $\nu \simeq 5 - 30$  Hz thanks to a finite synaptic time and to the self-inhibitory action of the neurons within the population.

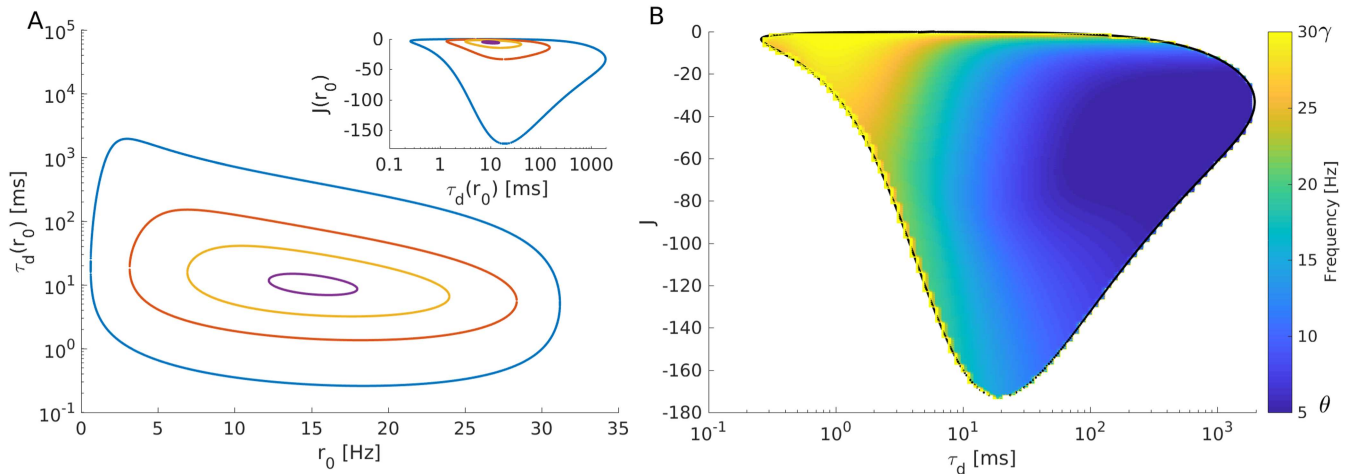


**FIG. 2.** Oscillation stability region: (a) Hopf bifurcation boundaries in the  $(r_0, \tau_d)$  plane obtained from (12) for four different values of the heterogeneity:  $\Delta = 0.01$  (blue),  $\Delta = 0.05$  (red),  $\Delta = 0.1$  (yellow),  $\Delta = 0.14$  (purple). Inset: Hopf bifurcation boundaries in the  $(\tau_d, J)$  space for the same  $\Delta$ -values. (b) Heat map of the frequencies of oscillation of the instantaneous firing rate in the  $(\tau_d, J)$  plane, for  $\Delta = 0.01$ . The black curve coincides with the Hopf boundary denoted in blue in the inset of panel (a). To quantify the frequencies of COs, a transient time  $t_t = 1$  s is discarded and then the number of peaks in  $r(t)$  are counted and divided by the simulation time  $t_s = 2$  s. For this figure,  $\tau = 10$  ms and  $\bar{\eta} = 1$ .

### B. One population under external forcing

Another relevant scenario in the framework of CFC<sup>31</sup> is the case in which an oscillatory drive  $I(t)$  is applied to a neural population exhibiting COs. The forcing term can represent an input generated from another neural population or an external stimulus. Therefore, we examine the behavior of the MF model driven by the following harmonic signal:

$$I(t) = -I_0(1 + \sin(2\pi\nu_0 t)), \quad (14)$$

characterized by a driving frequency  $\nu_0$  and an amplitude  $I_0$ . Note that we have chosen a strictly negative harmonic signal to assess the effect on the population dynamics of a driving signal originating from a distinct inhibitory population.

The results of this analysis are illustrated in Fig. 3. First, we study the phase locking of the population dynamics, characterized by an oscillatory frequency  $\nu$ , to the modulatory input, for different forcing frequencies  $\nu_0$  and amplitudes  $I_0$  [see Fig. 3(a)]. For small amplitudes, the external modulation is only able to lock the dynamics into a given  $n : m$  mode [measured in terms of the indicator (11)] for a limited range of forcing frequencies  $\nu_0$ , while the ratio  $n : m$  decreases for increasing  $\nu_0$ . Furthermore, the range where phase

locking is observable increases with the amplitude  $I_0$ , thus giving rise to the Arnold tongues shown in Fig. 3(a).

To better understand how the locking emerges, we consider the ratio  $\nu/\nu_0$  between the CO frequency and the forcing frequency for a large interval of  $\nu_0$ -values and for a fixed amplitude value  $I_0 = 0.4$ , denoted as a red dashed line in Fig. 3(a). The results are reported in Fig. 3(b). The ratio  $\nu/\nu_0$  reveals a structure similar to a devil's staircase, presenting plateaus (corresponding to the locked modes) intermingled with regions where the ratio does not always exhibit a monotonic behavior. For the same parameters, we also report the maxima  $r_{max}$  of the instantaneous firing frequency of the forced system and the corresponding Lyapunov Spectrum (LS) in Figs. 3(c) and 3(d), respectively. From these two indicators, one can infer that most of the phase-locked regions correspond to regular periodic motion, as revealed by the single value of  $r_{max}$  joined with the fact that  $\lambda_1 = 0$  and  $\lambda_2 < 0$  over a large portion of the devil's staircase plateaus. On the other hand, for  $\nu_0 > 15$  Hz the regions, where the  $r(t)$  presents peaks of different heights are in correspondence with the non-flat regions of the devil's staircase. In particular, these regions are associated with quasi-periodic motions, as confirmed by the existence of two zero LEs in the LS. A zoom in the region  $\nu_0 = [4, 14]$  Hz, corresponding to 1 : 1 locking, is reported

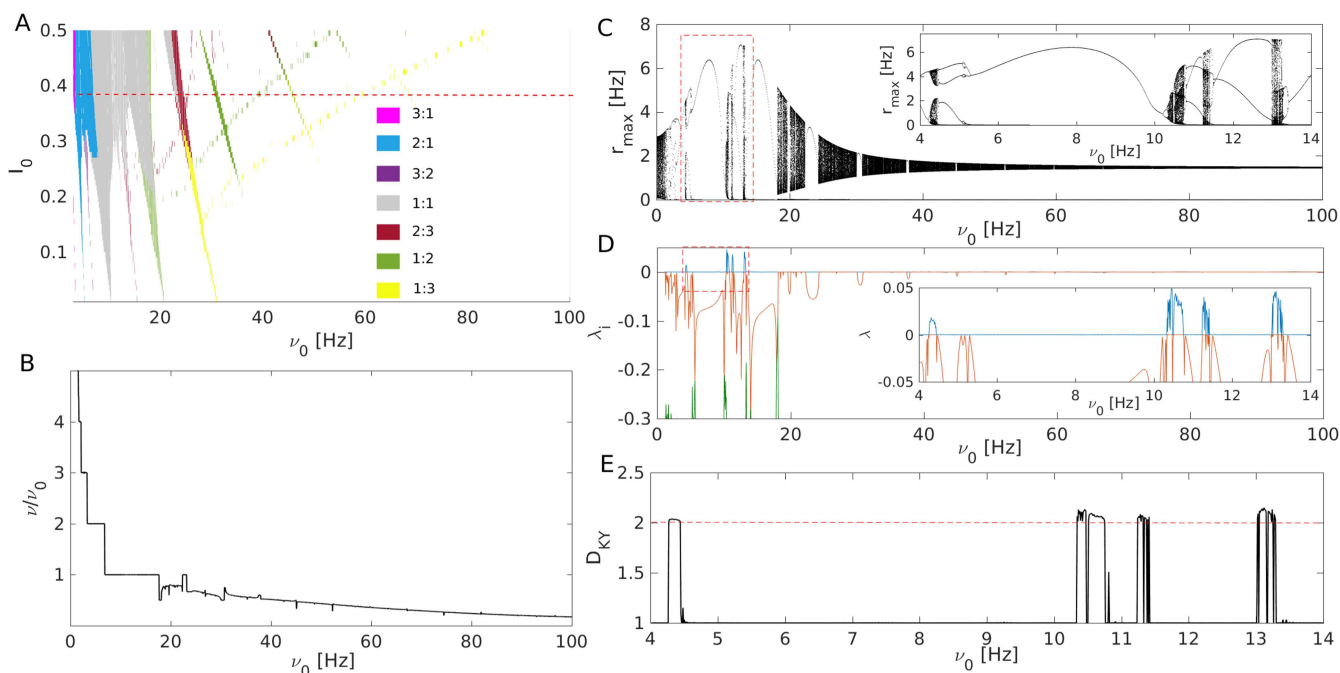


**FIG. 3.** Single population driven by a harmonic signal: (a) Phase locking diagram of a single inhibitory population driven by a purely inhibitory harmonic external drive (14) in the  $(I_0, \nu_0)$ -plane. Colors denote Arnold tongues with different phase locking ratios. The dashed line indicates the value  $I_0 = 0.4$  analyzed in the subsequent panels. (b) Ratio of the system's oscillation frequency  $\nu$  and of the driving frequency  $\nu_0$  as a function of  $\nu_0$ , showing a devil's staircase structure. Maxima of  $r$  (c) and the corresponding Lyapunov exponents (d) as a function of  $\nu_0$ . In particular, the first, second, and third LEs are reported as blue, red, and green lines, respectively. The dashed rectangles indicate the zoomed regions in (c) and (d) shown in the corresponding insets. (e) Kaplan–Yorke fractal dimension  $D_{KY}$  vs  $\nu_0$ . The dashed red line denotes a value of two. The employed parameters are  $J = -10$ ,  $\bar{\eta} = 1$ ,  $\Delta = 0.01$ ,  $\tau = 10$  ms, and  $\tau_d = 80$  ms. For the estimation of  $r_{max}$  and of the Lyapunov exponents, a transient time of  $t_t = 1$  s was discarded and then the maximum values were stored over a time interval  $t_s = 3$  s, while for the LS the tangent space was followed for a period  $t_s = 20$  s. The oscillation frequency of the unforced system is  $\nu = 10.4$  Hz.

in the insets of Figs. 3(c) and 3(d). These enlargements show the emergence of chaotic windows, where  $r_{\max}$  assumes values over continuous intervals and the maximal LE is positive. Furthermore, in these chaotic windows,  $D_{KY}$  is slightly larger than two, as shown in Fig. 3(e), indicating that the chaotic attractor is low dimensional. This is confirmed by the stroboscopic attractor reported in Fig. 4(b), obtained by reporting the macroscopic variables at regular time intervals equal to integer multiples of the forcing period  $\nu_0^{-1}$ .

Indeed, the points of the attractor cover a set with a dimension slightly larger than one, since one degree of freedom is lost due to the stroboscopic observation. Interestingly, the chaotic motion appears despite the 1:1 locking; this means that the time trace of  $r(t)$  always presents a single oscillation within a cycle of the external forcing but characterized by different amplitudes,<sup>52</sup> as shown in Fig. 4(a).

### C. Two populations in a master-slave configuration

Despite the fact that at a macroscopic level the network dynamics of a single population with exponential synapses is exactly described in the limit  $N \rightarrow \infty$  by three degrees of freedom (5), our and previous analyses<sup>24</sup> have not reported evidences of chaotic motions for a single inhibitory population. The situation is different for an excitatory population, as briefly discussed by Bi *et al.*,<sup>10</sup> or in the presence of external forcing as shown in Sec. III B.

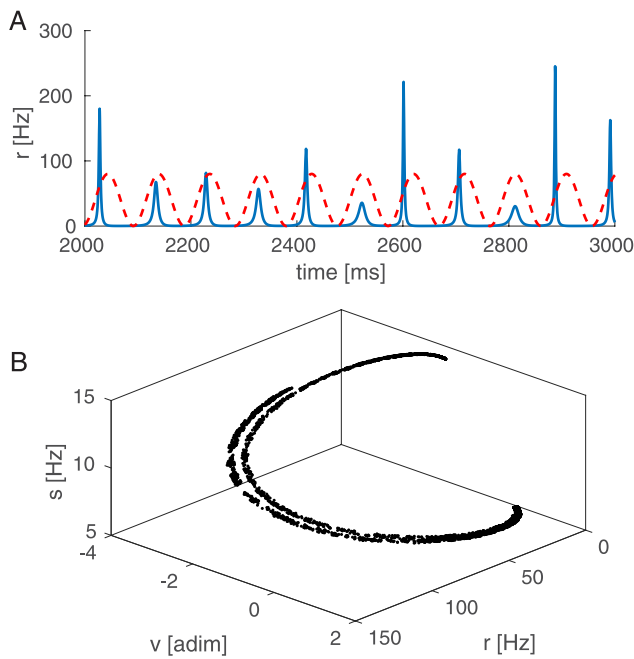


**FIG. 4.** Chaotic attractor for a single driven population: (a) Time trace of the average firing rate  $r(t)$  (blue solid line) and profile of the forcing term  $l(t)$  (red dashed line) are shown for a chaotic regime. The chaotic dynamics are clearly locked to the frequency of the external drive. (b) Stroboscopic attractor: the values of  $(r, v, s)$  are recorded at regular time intervals corresponding to integer multiples of the forcing period  $\nu_0^{-1}$ . Parameters for this figure as in Fig. 3 with  $\nu_0 = 10.4$  Hz.

In this subsection, we want to analyze the dynamical regimes emerging when a fast oscillating population (indicated as A) is driven by a slowly oscillating population (denoted by B) in a master-slave configuration corresponding to  $J_{BA} \neq 0$  and  $J_{AB} = 0$ . This is done in analogy with evidences found in the hippocampus, where an inhibitory population with slow synaptic kinetics projects toward interneurons with fast kinetics.<sup>6</sup> Particular attention will be devoted to chaotic regimes. An exhaustive parameter study has shown that the possible dynamical scenarios can be captured by the two parameter sets here analyzed, denoted as  $C_1$  and  $C_2$ ,

$$C_1 := \{\tau_d^{(A)} = 10 \text{ ms}, J_{AA} = -10, \tau_d^{(B)} = 50 \text{ ms}, J_{BB} = -16\},$$

$$C_2 := \{\tau_d^{(A)} = 2.5 \text{ ms}, J_{AA} = -10, \tau_d^{(B)} = 80 \text{ ms}, J_{BB} = -20\}.$$

In particular, we have considered parameter sets with biologically plausible synaptic time scales; indeed, they can correspond to populations of interneurons generating IPSPs mediated via  $GABA_{A,fast}$  and  $GABA_{A,slow}$  receptors, which have been identified in the hippocampus<sup>5</sup> and in the cortex.<sup>55</sup> The coupling between the two populations  $J_{BA}$  and the network heterogeneity  $\Delta = \Delta^{(A)} = \Delta^{(B)}$  will be employed as control parameters, while we will assume for simplicity  $\bar{\eta}^{(A)} = \bar{\eta}^{(B)} = 1$ .

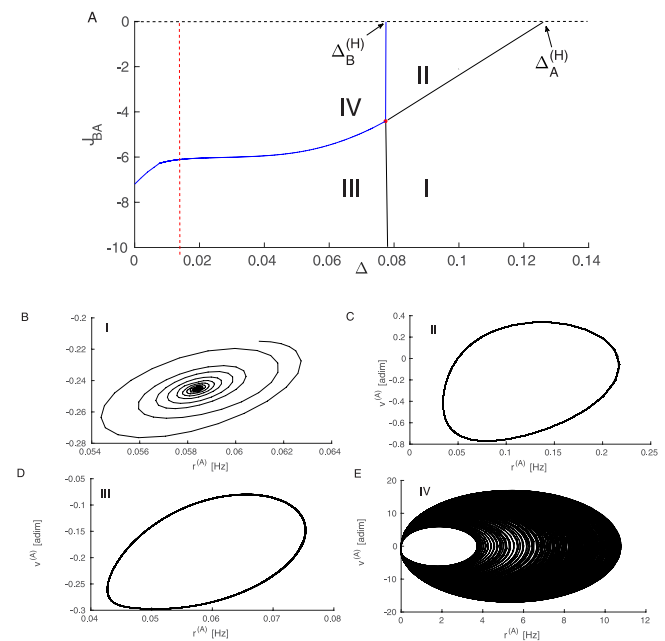


**FIG. 5.** Bifurcation diagram for the parameter set  $C_1$ . (a) Bifurcation diagram in the plane  $(\Delta, J_{BA})$  for the master-slave coupled system. The codimension 2 bifurcation point (red circle) divides the plane in four different regions (I–IV) corresponding to different dynamical regimes. The supercritical Hopf bifurcation points for the uncoupled populations A and B are denoted as  $\Delta_A^{(H)}$  and  $\Delta_B^{(H)}$  and indicated by the arrows. The Hopf bifurcations (black lines) separate foci from limit cycles, while the Torus bifurcations (blue lines) denote the emergence of  $T^2$  from limit cycles. A sample trajectory for each one of the four regions are shown in panels (b)–(e). The vertical red dashed line in (a) indicates the value of  $\Delta$  considered in Fig. 6.

Let us first consider the set of parameters  $C_1$ . In this case, the analysis of the possible bifurcations arising in the  $\{\Delta, J_{BA}\}$  plane reveals the existence of a codimension two bifurcation point at  $(\Delta^{(H)}, J_{BA}^{(H)}) \approx (0.078, -4.75)$ , namely, the intersection of two Hopf bifurcation lines, which organizes the plane into four different regions. In these regions, labeled I–IV, the prevalent dynamics corresponds to stable foci in I, stable limit cycles in II and III, and to stable Tori  $T^2$  in IV [see Fig. 5(a)]. For each region, we report in Fig. 5(b) a corresponding sample trajectory projected in the sub-space  $\{r^{(A)}, v^{(A)}\}$  taken in proximity of the codimension two point.

To better understand the emergence of the codimension two point, it is important to consider the uncoupled system, corresponding to  $J_{BA} = 0$  and depicted as a horizontal dashed line in Fig. 5(a). In this uncoupled regime, one expects to observe two independent supercritical Hopf bifurcations, one for each population, as discussed in Subsection III A. The first Hopf bifurcation, corresponding to the uncoupled fast population A, occurs at  $\Delta_A^{(H)} \approx 0.122$  while the second one, associated with the slow uncoupled population B, is located at  $\Delta_B^{(H)} \approx 0.078$ . Obviously, since the coupling is unidirectional from population B to A, the locus of the Hopf bifurcations emerging at  $\Delta_B^{(H)}$  is not influenced from the value of  $J_{BA}$  and it corresponds to a vertical line  $\Delta^{(H)} \equiv \Delta_B^{(H)}$  in the  $\{\Delta, J_{BA}\}$  plane. Conversely, as population A is forced by the activity of population

B, the Hopf curve emerging from  $\Delta_A^{(H)}$  has a dependence on the  $J_{BA}$  coupling that leads this bifurcation curve to cross the line  $\Delta^{(H)}$  in the codimension two point. Therefore, the vertical Hopf  $\Delta^{(H)}$  line divides foci (I) from stable oscillations (III) for  $J_{BA} < J_{BA}^{(H)}$ , while at larger coupling  $J_{BA}$ , it becomes a secondary Hopf (or Torus) bifurcation line (blue solid), separating periodic (II) from quasi-periodic motions (IV). Moreover, the region III of stable limit cycles is divided by region IV, where Tori  $T^2$  emerge from another Torus bifurcation line (blue solid).

We will now focus on the case  $\Delta = 0.01$  [corresponding to the red dashed line in Fig. 5(a)] to analyze the different regimes observable by varying  $J_{BA}$ . To this aim, similarly to what was done in Sec. III B, we characterize the dynamics of the system in terms of the values of the Poincaré map  $r_{max}^{(A)}$  and of the associated LS. In particular, in Fig. 6(a) are reported the values of  $r_{max}^{(A)}$  in the range of cross-inhibition  $J_{BA} = [-10, 0]$ . At very negative values of the cross-coupling, we observe a single value for  $r_{max}^{(A)}$ , which corresponds to periodic COs. This is confirmed by the values of the LS reported in Fig. 6(b): the LEs are all negative except for the first one, which is zero. At  $J_{BA} \approx -6.05$ , a broad band appears for the distribution of  $r_{max}^{(A)}$ , indicating that the time trace now displays maxima of different heights. This is due to the Torus bifurcation leading from a periodic to a quasi-periodic motion. The emergence of quasi-periodic motions is confirmed by the fact that in the corresponding

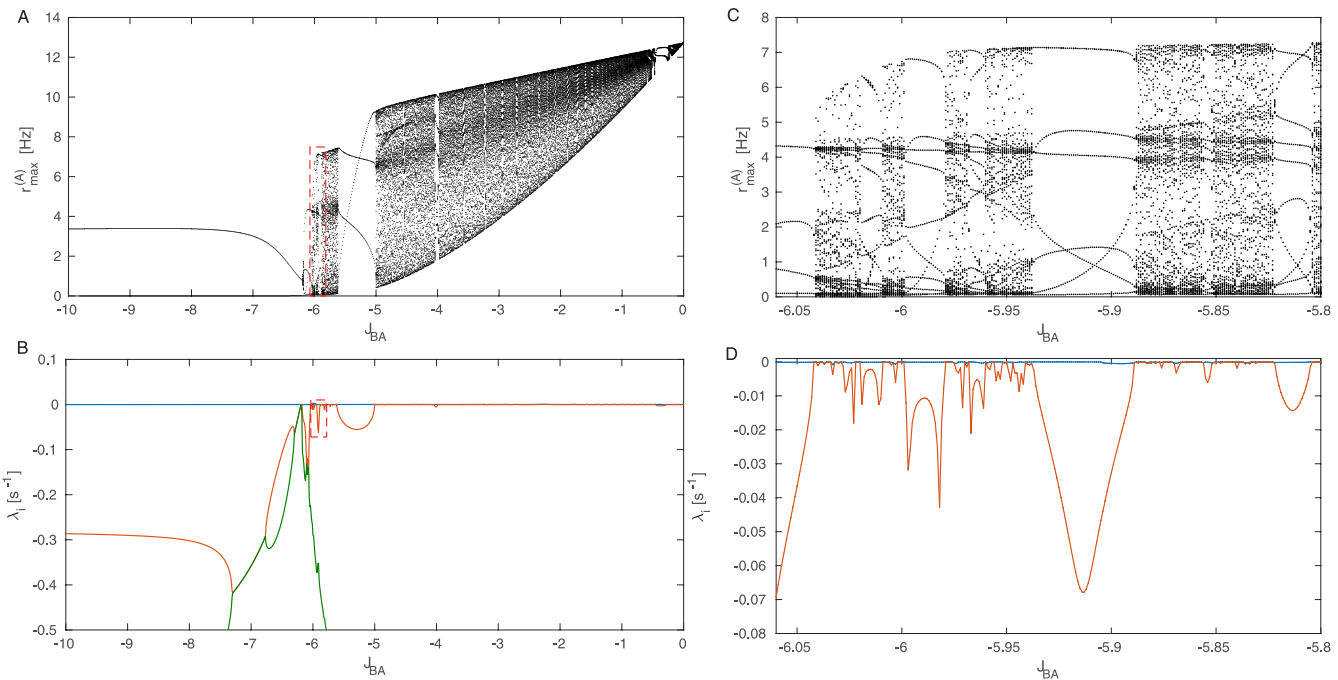


**FIG. 6.** Characterization of the dynamics for the parameter set  $C_1$ . (a) and (c) Local maxima  $r_{max}^{(A)}$  of the firing rate of the populations (A) and (B), (d) LEs as a function of the coupling strength  $J_{BA}$ . In panels (b) and (d), the blue curve represents the first LE, the orange the second LE, and the green one the third LE. The dashed rectangle in panels (a) and (b) indicate the zoomed region presented in panels (c) and (d). For the evaluation of the maxima, a transient time of  $t_t = 10$  s was discarded and then maximum values were stored during  $t_s = 15$  s. For the LEs estimation, after discarding the transient time  $t_t$ , the evolution of the tangent space was followed for a period  $t = 500$  s.



intervals, the first two LEs are zero [Fig. 6(d)]. For larger values of the cross-coupling (namely,  $J_{BA} \approx [-5.8 : -5]$ ), a period three window is clearly observable. Beyond this interval, one observes quasi-periodic motions for almost all the negative values of the cross-coupling, apart from narrow parameter intervals where locking of the two frequencies of the COs occur, as expected beyond a Torus bifurcation.<sup>37</sup>

We then proceed to study the parameter set  $C_2$ . First, we show that the bidimensional bifurcation diagram in the plane  $\{\Delta, J_{BA}\}$  presents a similar structure to that reported in Fig. 5(a). Indeed, also in the present case, a codimension two point located at  $\{\Delta^{(H)}, J_{BA}^{(H)}\} \approx \{0.06, 0\}$  divides the phase space in four regions analogous to those observed for the parameter set  $C_1$  and separated by the same kind of bifurcations [see the inset of Fig. 7(a)]. As in the previous case, we select the value  $\Delta = 0.01$  for analyzing the distribution of maxima of the firing rate  $r^{(A)}$  and the associated Lyapunov spectra (see Fig. 7). For highly negative values of the cross-inhibition, we observe a periodic behavior of the firing rate  $r^{(A)}$ . At the intersection with the torus bifurcation (occurring at  $J_{BA} = -7.48$ ), quasi-periodicity emerges similarly to what observed for the parameter set  $C_1$ . However, at larger values of the cross-inhibition (namely,  $J_{BA} \in [-7.3445, -7.3217]$ ), we observe a period-doubling cascade leading to chaos for  $J_{BA} \simeq -7.32$ . The system remains chaotic in the interval  $J_{BA} \in [-7.32, -7.18]$  apart from the occurrence of periodic

windows. This is confirmed by the fact that the maximal LE becomes positive in the corresponding interval, as shown in Fig. 7(d). An example of chaotic attractor is reported in Fig. 7(f) with a fractal dimension slightly larger than two, as confirmed by the estimation of  $D_{KY}$  presented in Fig. 7(e). As in the case of the single forced population, the macroscopic chaotic attractor is low dimensional. For  $J_{BA} > -7.18$ , we have periodic and quasi-periodic activity, but no more chaos. In particular, for  $J_{BA} > -4.2$ , we essentially observe mostly quasi-periodic motions up to  $J_{BA} = 0$ .

Although we have been able to find chaotic bands for other sets of parameters, we have preferred to focus on a case where the synaptic time scale of the master population  $\tau_d^{(B)}$  is of the order of the kinetics expected for IPSPs mediated via  $GABA_{A,slow}$  receptors.<sup>5,55</sup>

### D. Cross-frequency-coupling in bidirectionally coupled populations

As previously mentioned, a fundamental example of CFC is represented by the coupling of the  $\theta$  and  $\gamma$  rhythms. Gamma oscillations are usually modulated by theta oscillations during locomotory actions and rapid eye movement (REM) sleep in the hippocampus<sup>40</sup> as well as in the neocortex.<sup>56</sup> While gamma oscillations have been shown to be crucially dependent on inhibitory networks,<sup>17</sup> the origin of the  $\theta$ -modulation is still under debate. It has been suggested to be

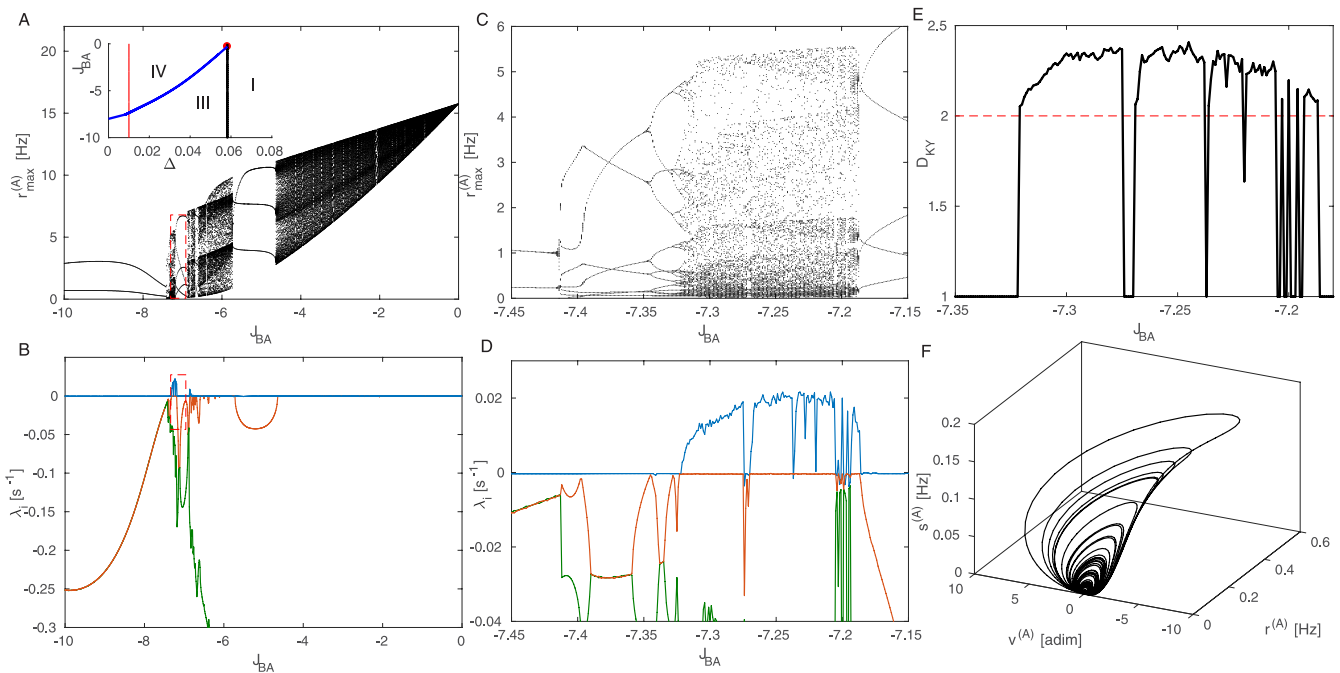


**FIG. 7.** Characterization of the dynamics for the parameter set  $C_2$ . (a) and (c) Values of  $r_{max}^{(A)}$  as a function of  $J_{BA}$ . The inset shows the bifurcation diagram in the  $(\Delta, J_{BA})$  plane. This reveals the same structure as the diagram in Fig. 5(a). Here, region (II) is not shown since it corresponds to the region of excitatory cross-coupling. (b) and (d) First three LEs as a function of cross-inhibitory coupling  $J_{BA}$ . The red dashed rectangles in panels (a) and (b) denote the zoomed regions presented in panels (c) and (d), respectively. (e) Kaplan–Yorke dimension  $D_{KY}$  in the parameter interval where chaos is present. (f) Chaotic attractor in the  $(r^{(A)}, v^{(A)}, s^{(A)})$  space at  $J_{BA} = -7.25$ . For the evaluation of  $r_{max}^{(A)}$ , a transient time of  $t_t = 10$  s was discarded and then maximal values were stored during  $t_s = 15$  s. For the LEs estimation, after the same transient time as before, the evolution of the tangent space was followed during  $t = 50$  s.

due either to an external excitatory drive<sup>15</sup> or to a cross-disinhibition originating from a distinct inhibitory population.<sup>29,61</sup>

In this subsection, we analyze the possibility that two bidirectionally interacting inhibitory populations could be at the basis of the  $\theta$ - $\gamma$  CFC. Inspired by previous analysis, we propose the difference in the synaptic time kinetics as a possible mechanism to achieve CFC.<sup>61</sup> Therefore, we set the synaptic time scales of the fast and slow populations to  $\tau_{A,d} = 9$  ms ( $\tau_{B,d} = 50$  ms), which correspond approximately to the time scales of IPSPs generated via GABA<sub>A,fast</sub> (GABA<sub>A,slow</sub>) receptors. Regarding the other parameters internal to each population, these are chosen in a such a way that the self-generated oscillations correspond roughly to  $\theta$  and  $\gamma$  rhythms, respectively.

First, we consider the case in which no external modulation is present, i.e.,  $I^{(l)}(t) = 0$ . Depending on the value of the cross-coupling parameters  $J_{AB}$  and  $J_{BA}$ , different types of  $m:n$  P-P coupling can be achieved. In particular, as shown in Fig. 8(a), we observe 1:1 and 2:1 phase synchronization in large regions of the  $(J_{AB}; J_{BA})$  plane, while 3:1 and 5:2 locking emerge only along restricted stripes of the plane. In particular, we focus on the values of cross-inhibition  $J_{lk}$  for which it is possible to achieve a 3:1 phase synchronization, corresponding to a  $\theta$ - $\gamma$  coupling. As evident from the green area in

Fig. 8(a), this specific P-P coupling occurs only for low values of  $J_{AB}$ , namely,  $J_{AB} \in [0.5, 2.5]$ .

Among the parameter values corresponding to 3:1 locking, we choose for further analysis the ones for which the order parameter  $\rho_{31}$  is maximal [denoted as a red circle in Fig. 8(a)]. In particular, we performed simulation of the network (1) as well as of the corresponding MF model (5). The raster plot in Fig. 8(b) confirms that the two populations display COs locked in a 3:1 fashion. During the burst emitted from the slow population, the fast displays irregular asynchronous activity followed by three rapid bursts (each lasting around 10 ms), before the next CO of the slow population. The fact that the slow population emits bursts of longer duration is confirmed by the analysis of the instantaneous firing rates reported in Fig. 8(d). Indeed,  $r^{(A)}$  has oscillations of much greater amplitude than  $r^{(B)}$ , indicating that more neurons are recruited for a burst of population A with respect to population B. This difference in the oscillation amplitude can also explain why the 3:1 locked mode is observable for  $J_{AB} \ll J_{BA}$ ; indeed, for larger  $J_{AB}$ , the activity of the slow population would be silenced. It is worth noticing in Figs. 8(b) and 8(c) the strong agreement between the firing rates obtained from the network simulations (dots) and from the evolution of the MF model (line).

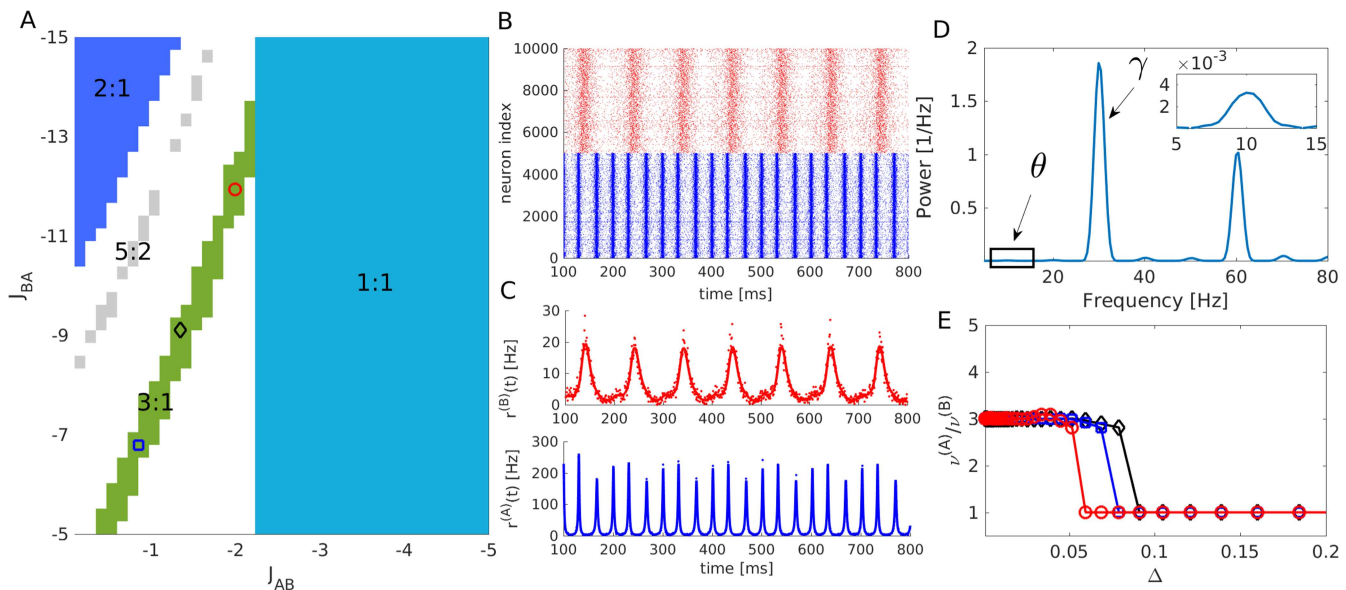


**FIG. 8.** CFC in bidirectionally coupled populations. (a) Heat map of the order parameter locking modes for different values of the cross-coupling. Colored symbols denote three pairs of parameters  $\{J_{AB}, J_{BA}\}$  corresponding to 3:1 locking examined in (e) for different disorder values. In particular the red circle denotes the couple  $\{J_{AB}, J_{BA}\}$  for which one obtains the maximal value of  $\rho_{31}$  and these parameter values are employed for the simulations reported in (b) and (c). (b) Raster plot of the network model Eq. (1) showing the fast and slow population in blue and red colors, respectively. (c) Instantaneous firing rates of the two populations obtained from the evolution of the MF dynamics (5) [same color code as in panel (b)]. (d) Power spectrum of the time trace  $r^{(A)}(t)$  shown as a blue line in panel (c). In the inset, an enlargement of the spectrum corresponding to the  $\theta$ -band is shown. (e) Ratio of the fast and slow frequencies of the COs  $\nu^{(A)}/\nu^{(B)}$  vs the disorder  $\Delta := \Delta_A = \Delta_B$ . The ratio shows the extent of the 3:1 locking interval for the three values of  $\{J_{AB}, J_{BA}\}$  denoted by the symbols of the same color in (a). Parameters for fast population are  $\tau_d^{(A)} = 9$  ms,  $\bar{\eta}_A = 2$ ,  $J_{AA} = -2$  and for the slow one  $\tau_d^{(B)} = 50$  ms,  $\bar{\eta}_B = 1.5$ ,  $J_{BB} = -18$ . Common parameters:  $\Delta = 0.05$  [for panels (a)–(d)] and  $\tau = 10$ . The time traces used for the phase locking analysis were taken over a period of  $t = 10$  s after discarding an initial transient time  $t_t = 10$  s. For the network simulations in (b),  $N_A = N_B = 10\,000$  neurons. In the figure, only half of them are depicted. The spectrum in (d) was obtained by averaging 50 power spectra, each calculated over a time trace of duration  $t = 16.384$  s with  $2^{15}$  equispaced samples, after a transient time of  $t_t = 10$  s.

An analysis of the power spectrum of  $r^{(A)}$  [shown in Fig. 8(d)] reveals that the amount of power in the  $\theta$  band is quite small (see the peak around 10 Hz in the inset) with respect to the power in the  $\gamma$  band. This indicates that a CFC among the two bands is indeed present, but the interaction is limited.

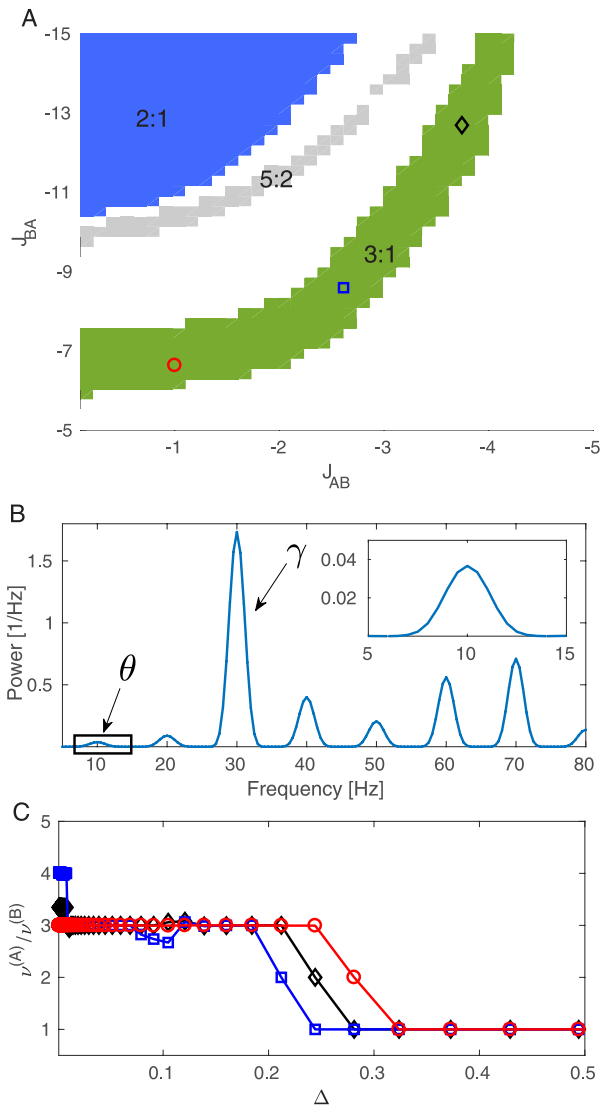


**FIG. 9.** CFC in bidirectionally coupled populations with an external  $\theta$  modulation. (a) Locking modes for different values of the cross-coupling. Red circle denotes the pair  $\{J_{AB}, J_{BA}\}$  giving rise to the maximum value of  $\rho_{31}$  which is used for simulations in (b)–(c). Black diamond and blue square correspond also to 3:1 modes with a smaller order parameter value. (B) Power spectrum of the time trace  $r^{(A)}(t)$  for the case denoted by the red circle in panel (a). The inset displays an enlargement corresponding to the  $\theta$ -band. (C) Ratio of the fast and slow population frequencies  $\nu^{(A)}/\nu^{(B)}$  showing the extent of the 3:1 mode for the three values of  $\{J_{AB}, J_{BA}\}$  depicted by the symbols in (a) at varying values of disorder  $\Delta := \Delta^{(A)} = \Delta^{(B)}$ . For the  $\theta$ -forcing current, we set  $I_0^{(B)} = 0.5$  and  $\nu_\theta = 10$  Hz, all the other parameters as in Fig. 8.

Furthermore, varying the amplitude of the heterogeneity, as measured by  $\Delta = \Delta^{(A)} = \Delta^{(B)}$ , we can verify the capability of the network to sustain the 3:1 locked mode even in the presence of disorder in the neural excitabilities. It can be seen that the system loses the ability to sustain such a locked state already for  $\Delta > 0.1$ , indicating that CFC can occur only for a limited amount of disorder in the distribution of the neuronal excitabilities in agreement with the results reported by White *et al.*<sup>61</sup> [see Fig. 8(e)]. For large disorders, the only possible locked state is that corresponding to 1:1 phase synchronization.

So far, we have analyzed the possibility that  $\theta$  and  $\gamma$  rhythms were locally generated in inhibitory populations with different synaptic scales. However, the results of several optogenetic experiments performed in different areas of the hippocampus and entorhinal cortex suggest that a  $\theta$  frequency drive is sufficient to induce *in vitro*  $\theta$ – $\gamma$  CFCs.<sup>3,13,14,50</sup> However, the interpretation of these experiments disagrees on the origin of the locally generated  $\gamma$  oscillations. Two mechanisms have been suggested: namely, either inhibitory<sup>3,50</sup> or excitatory–inhibitory feedback loops.<sup>13,14</sup> Therefore, to clarify if recurrently coupled inhibitory populations with different synaptic time scales under a  $\theta$ -drive can display  $\theta$ – $\gamma$  CFC, we drive the slow population via an external current  $I^{(B)} = I_0^{(B)} \sin(2\pi \nu_\theta t)$  with  $\nu_\theta = 10$  Hz, while the rest of the parameters remains unchanged.

As before, we look for the range of cross-inhibitions in which a 3:1 phase-locked mode emerges. Results are plotted in Fig. 9(a). We observe that the region where  $\theta$ – $\gamma$  CFC can be observed definitely enlarges in the presence of an external  $\theta$ -modulation. Furthermore, as observable from the power spectrum reported in Fig. 9(b), the

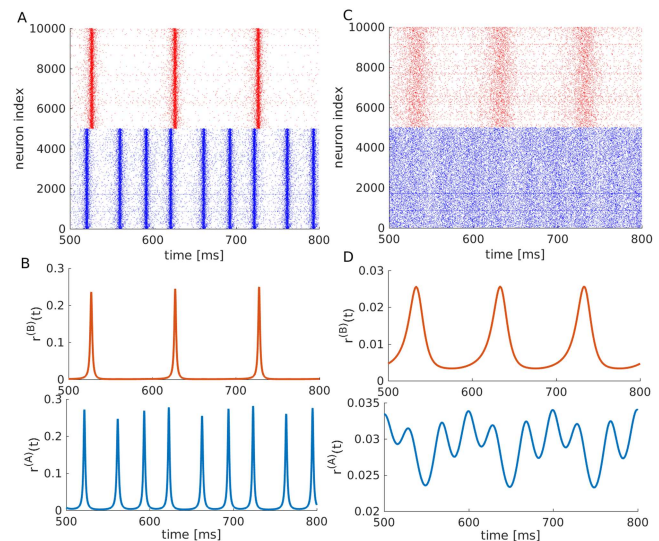


**FIG. 10.** P–P and P–A couplings in the presence of a  $\theta$  forcing. (a) Raster plot of the network model Eq. (1) showing the fast and slow population in blue and red colors, respectively, for the same system analyzed in Fig. 9 with the optimal pair  $\{J_{AB}, J_{BA}\} = \{-1, -6.63\}$  and  $\Delta = 0.05$ . (b) Time traces of  $r(t)$  for the fast (blue) and slow (red) populations for the case depicted in the raster plot in (a). (c)–(d) Same as in (a)–(b) for the same parameters except for  $\Delta = 0.2$ . Parameters as in Fig. 9.

power in the  $\theta$  band is noticeably increased as a consequence of the external modulation with respect to the non-modulated case. Moreover, the  $\theta$ - $\gamma$  CFC is now observable over a wider range of disorder on the excitabilities; indeed, the 3:1 locked state survives up to  $\Delta \approx 0.2$ – $0.3$ , as shown in Fig. 9(c). These findings are consistent with those previously reported by White *et al.*,<sup>61</sup> in which adding a slow modulation to the  $\theta$ -generating population was sufficient to render more robust the observed CFC to the presence of disorder in the excitability distribution.

Finally, if we consider the network activity, we observe two different scenarios corresponding to the 3:1 locked mode: (1) a P–P locking at low disorder and (2) a P–A coupling (or  $\theta$ -nested  $\gamma$  oscillations) at larger disorder. The first scenario is characterized by the fast population displaying clear COs slightly modulated in their amplitudes by the activity of the slow population, but tightly locked in phase with the slow ones [see Figs. 10(a) and 10(b)]. The second scenario presents a firing activity of the fast population strongly modulated in its amplitude by the slow population as observable in Figs. 10(a) and 10(b). In this latter case, the neurons in population A fire almost asynchronously with a low firing rate, thus the forcing of the slow population B on the fast one A is reduced with respect to the previous case. However, the coupling with the activity of the slow population B is reflected in a clear modulation of the firing rate  $r^{(A)}$ , analogously to what has been reported for  $\theta$ -nested  $\gamma$  oscillations induced by optogenetic stimulation.<sup>14,50</sup>

#### IV. CONCLUDING REMARKS

In this paper, we have considered a heterogeneous inhibitory population with exponentially decaying synapses, which can be described at a macroscopic level by an exact reduced model of three variables: the firing rate, the average membrane potential, and the mean synaptic activity. As demonstrated previously by Coombes *et al.*<sup>21</sup> and Devalle *et al.*,<sup>24</sup> the presence of the synaptic dynamics is at the origin of the COs, emerging via a super-critical Hopf bifurcation. In particular, we have shown that the period of the COs is controlled by the synaptic time scale and that, for increasing heterogeneity, the observation of COs requires finer and finer tuning of the model parameters. Moreover, we have characterized in detail the effect of an inhibitory periodic current on a single self-oscillating population. The external forcing leads to the appearance of locking phenomena characterized by Arnold tongues and devil's staircase. We have also identified chaotic windows, where the instantaneous firing rate of the forced population display oscillations which are irregular in amplitude, but tightly locked in frequency to the external signal oscillations.<sup>52</sup>

Furthermore, we considered two inhibitory populations connected in a master–slave configuration, i.e., unidirectionally coupled, where the fast oscillating population is forced by the one with slower synaptic dynamics. For a single uncoupled population, we observe focus solutions at large heterogeneity  $\Delta$ , which give rise to collective oscillations via a super-critical Hopf bifurcation at lower  $\Delta$ . Clearly, the scenario becomes more complex by considering two coupled populations. In particular, we observe four distinct dynamical regimes organized around a codimension two bifurcation point: namely, the observed dynamics correspond

to foci, periodic, and quasi-periodic motions. Each region is separated by the others via super-critical Hopf or Torus bifurcation lines. Depending on the parameter values, a period doubling cascade leading to chaotic behavior is observable just above the Torus bifurcation from periodic to quasi-periodic dynamics. In particular, the corresponding chaotic attractor is quite low-dimensional, with a fractal dimension slightly larger than two and a single positive Lyapunov exponent, despite the fact that the two coupled neural mass models are described by six degrees of freedom. The macroscopic solutions we have found in the master–slave configuration are similar to those identified by Luke *et al.*<sup>44</sup> for  $\theta$ -neurons populations coupled via pulses of finite width.

Even though the dichotomy between chaos and reliability in brain coding is a debated topic,<sup>4,32,38,41</sup> it is of great importance to establish the microscopic or collective nature of such behavior, as well as the conditions of its occurrence. Here, we focused on the emergence of collective chaos, i.e., chaos at the level of population dynamics, in networks of simple neuronal models that are not independently chaotic. Collective chaos has been reported in single globally coupled heterogeneous populations in the presence of an external time scale, which can be due to an (effective) delay<sup>23,42,59</sup> or a periodic forcing.<sup>44,57</sup> In the present work, we have shown that collective chaos can be considered as a further example of cross-frequency coupling between two oscillating neural populations in a master–slave configuration, or in a single oscillating population locked to an external sinusoidal forcing. The functional role of this chaotic cross-frequency-coupling for the brain activity is an open problem that deserves further experimental and theoretical analysis.

We finally explored the possibility that two mutually interacting inhibitory networks could give rise to  $\theta$ - $\gamma$  CFC emerging as a consequence of the interaction between fast and slow GABA<sub>A</sub> kinetics.<sup>61</sup> In the original setup,  $\theta$ - $\gamma$  CFC coupling was observed only in a narrow region of parameters and for a limited range of heterogeneity. The addition of a  $\theta$ -forcing on the slow population renders the system more robust to the disorder in the excitability distribution and enlarges the observability region of the  $\theta$ - $\gamma$  CFC. Furthermore, we observed two kinds of CFCs: P–P (P–A) coupling for low (high) heterogeneity. It is interesting to notice that P–P coupling emerges only when the slow population is sufficiently synchronized to exert a strong forcing on the fast population, while for weaker synchronization (forcing) the P–A coupling is observable. This result is analogous to what recently found for a single sparse inhibitory population under external periodic forcing.<sup>10</sup> Both of these scenarios have been reported experimentally for  $\theta$ - $\gamma$  oscillations: P–A coupling has been reported *in vitro* for optogenetic  $\theta$ -stimulations of the hippocampal areas CA1<sup>14</sup> and CA3,<sup>3</sup> as well as of the medial entorhinal cortex;<sup>50</sup> P–P coupling has been observed in the hippocampus of behaving rats.<sup>8,20</sup>

Our analysis shows, for the first time to our knowledge, that the  $\theta$ - $\gamma$  CFC reported for two globally coupled inhibitory populations of Hodgkin–Huxley neurons by White *et al.*<sup>61</sup> can be reproduced at the level of exact neural mass models. Furthermore, our findings indicate that the mechanism responsible of  $\theta$ - $\gamma$  CFC in two coupled inhibitory populations is quite general, since this emerges in networks of conductance-based class II neurons,<sup>61</sup> as well as for current-driven class I neurons. Our results pave the way for further studies of other CFC mechanisms present in the brain, e.g.,



by employing analytically estimated macroscopic phase response curves<sup>26</sup> to characterize phase synchronization in multiscale networks of QIF neurons.

A further relevant step in the development of realistic mean-field models for neural systems is to extend the approach here discussed to sparse networks, where COs can emerge due to unavoidable endogenous fluctuations.<sup>11,12,25</sup> In this context, the MF description has been successfully achieved in terms of the corresponding Fokker–Planck equation for the distribution of the membrane potentials.<sup>11,12,19,58</sup> This MF framework allows us to include, in the macroscopic formulation, the effect of the fluctuations present in the microscopic dynamics. However, it comes with the downside of the high-dimensionality of the model, since the MF dynamics can be obtained by solving a partial differential equation. An extremely relevant challenge is to derive exact low dimensional neural mass models for sparse networks: first attempts in this direction have been reported in Refs. 25 and 10. However, in these works, the sparseness is treated as a source of quenched disorder in the network, thus lacking the inclusion of the dynamical effects related to the random distribution of the in-degrees. A promising approach in this direction is represented by the application of circular cumulant reductions to obtain the macroscopic dynamics of coupled QIF neurons.<sup>28,53</sup>

## ACKNOWLEDGMENTS

The authors are in debt to Ernest Montbrió for various enlightening interactions in the first phase of development of this project; furthermore, they acknowledge fruitful discussions with Federico Devalle, Boris Gutkin, and Alex Roxin. A.T. received financial support from the Excellence Initiative A\*MIDEX (Grant No. ANR-11-IDEX-0001-02) (together with D.A.-G.), the Excellence Initiative I-Site Paris Seine (Grant No. ANR-16-IDEX-008), the Labex MME-DII (Grant No. ANR-11-LBX-0023-01) (together with S.O.) and the ANR Project ERMUNDY (Grant No. ANR-18-CE37-0014), which are all part of the French programme “Investissements d’Avenir.” D.A.-G. was also supported by CNRS for a research period at LPTM, UMR 8089, Université de Cergy-Pontoise, France. A.C. was supported by Erasmus+ Traineeship 2016/2017 Contract between University of Florence, Department of Mathematics and Computer Science “Ulisse Dini” (DIMAI), and Centre de Physique Théorique (CPT) and LabEx Archimède, Marseille, France. D.A.-G. also received partial support from Vicerrectoria de Investigaciones - Universidad de Cartagena (Project No. 085-2018).

## APPENDIX: HOPF BOUNDARIES

In the case of a single population of inhibitory neurons with no external input, the fixed point solutions  $(v_0, r_0, s_0)$  of MF model (5) are given by the following set of equations:

$$v_0 = -\frac{\Delta}{2\tau\pi r_0}, \quad (\text{A1})$$

$$v_0^2 + \bar{\eta} - (\pi\tau r_0)^2 + \tau J s_0 = 0, \quad (\text{A2})$$

$$s_0 = r_0. \quad (\text{A3})$$

In order to study the linear stability of the equilibrium point, we consider the corresponding eigenvalue problem, namely,

$$\det \begin{bmatrix} 2v_0/\tau - \Lambda & 2r_0/\tau & 0 \\ -2\pi^2\tau r_0 & 2v_0/\tau - \Lambda & J \\ 1/\tau_d & 0 & -\Lambda - 1/\tau_d \end{bmatrix} = 0, \quad (\text{A4})$$

where  $\Lambda$  are the complex eigenvalues which can be found by solving the following characteristic polynomial:

$$p(\Lambda) = \tau_d \tau^2 \Lambda^3 + A \Lambda^2 + \Lambda (\tau_d B - 4\tau v_0) + (B - 2r_0 J \tau), \quad (\text{A5})$$

where  $A = (\tau^2 - 4v_0\tau_d\tau)$  and  $B = (4v_0^2 + 4\pi^2 r_0^2 \tau^2)$ .

In order to obtain a parameterization of the Hopf bifurcation curve, we impose  $\Lambda = i\Omega$  with  $\Omega \in \mathfrak{R} \setminus \{0\}$  and solve  $p(i\Omega) = 0$ , which can only be satisfied if

$$\text{Re}[p(i\Omega)] = 0 \quad \text{and} \quad \text{Im}[p(i\Omega)] = 0. \quad (\text{A6})$$

Solving for  $\Omega$  in Eqs. (A6), we end up with

$$\Omega_{\text{Re}} = \pm \sqrt{\frac{(B - 2r_0 J \tau)}{A}}, \quad (\text{A7})$$

$$\Omega_{\text{Im}} = \pm \sqrt{\frac{(\tau_d B - 4\tau v_0)}{\tau_d \tau^2}}. \quad (\text{A8})$$

By equating (A7) and (A8) we can find the values of  $J^{(H)}$ , where the Hopf bifurcation occurs, namely,

$$J^{(H)} = \frac{2v_0 [\tau^2 (4\pi^2 \tau_d^2 r_0^2 + 1) + 4\tau_d^2 v_0^2 - 4\tau_d \tau v_0]}{\tau_d r_0 \tau^2}. \quad (\text{A9})$$

Finally, by introducing Eqs. (A9) in (A2), and noticing from Eq. (A3) that  $s_0 = r_0$ , one can derive the values of the synaptic time scale  $\tau_d^{(H)}$  that bounds the oscillating region and that is reported in Eq. (12). Notice that the dependence on  $\Delta$  is implicitly introduced in the expression of  $v_0$ ; therefore it is possible to obtain also the critical value  $\Delta^{(H)}$  associated with the Hopf transition by substituting (A1) in (A2) and solving for  $\Delta$ . It should be stressed that this approach cannot distinguish between super-critical and sub-critical Hopf bifurcations. As a matter of fact, for an inhibitory QIF population with exponential synapses no sub-critical bifurcations have been reported for homogeneous synaptic couplings,<sup>24</sup> while these emerge whenever a disorder is introduced either in the synaptic couplings or in the link distribution.<sup>10</sup>

## REFERENCES

- <sup>1</sup>GABA (gamma-aminobutyric acid) is the main inhibitory neurotransmitter in the adult mammalian brain. GABA performs its action by binding to GABA<sub>A</sub> or GABA<sub>B</sub> receptors.
- <sup>2</sup>For what concerns the cases with an external forcing (i.e., non-autonomous systems), we have chosen to consider the time as an extra independent variable, therefore, to treat the system as autonomous, with an additional degree of freedom.
- <sup>3</sup>T. Akam, I. Oren, L. Mantoan, E. Ferenczi, and D. M. Kullmann, “Oscillatory dynamics in the hippocampus support dentate gyrus–CA3 coupling.” *Nat. Neurosci.* **15**(5), 763 (2012).



- <sup>4</sup>D. Angulo-Garcia and A. Torcini, "Stable chaos in fluctuation driven neural circuits," *Chaos Solitons Fractals* **69**(0), 233–245 (2014).
- <sup>5</sup>M. I. Banks, T. -B. Li, and R. A. Pearce, "The synaptic basis of GABAA, slow," *J. Neurosci.* **18**(4), 1305–1317 (1998).
- <sup>6</sup>M. I. Banks, J. A. White, and R. A. Pearce, "Interactions between distinct GABAA circuits in hippocampus," *Neuron* **25**(2), 449–457 (2000).
- <sup>7</sup>W. Bao and J.-Y. Wu, "Propagating wave and irregular dynamics: Spatiotemporal patterns of cholinergic theta oscillations in neocortex *in vitro*," *J. Neurophysiol.* **90**(1), 333–341 (2003).
- <sup>8</sup>M. A. Belluscio, K. Mizuseki, R. Schmidt, R. Kempter, and G. Buzsáki, "Cross-frequency phase-phase coupling between theta and gamma oscillations in the hippocampus," *J. Neurosci.* **32**(2), 423–435 (2012).
- <sup>9</sup>G. Benettin, L. Galgani, A. Giorgilli, and J.-M. Strelcyn, "Lyapunov characteristic exponents for smooth dynamical systems and for hamiltonian systems; a method for computing all of them. Part 1: Theory," *Meccanica* **15**(1), 9–20 (1980).
- <sup>10</sup>H. Bi, M. Segneri, M. di Volo, and A. Torcini, "Coexistence of fast and slow gamma oscillations in one population of inhibitory spiking neurons," *Phys. Rev. Res.* **2**(1), 013042 (2020).
- <sup>11</sup>N. Brunel, "Dynamics of sparsely connected networks of excitatory and inhibitory spiking neurons," *J. Comput. Neurosci.* **8**(3), 183–208 (2000).
- <sup>12</sup>N. Brunel and V. Hakim, "Fast global oscillations in networks of integrate-and-fire neurons with low firing rates," *Neural Comput.* **11**(1), 1621–1671 (1999).
- <sup>13</sup>J. L. Butler, Y. A. Hay, and O. Paulsen, "Comparison of three gamma oscillations in the mouse entorhinal-hippocampal system," *Eur. J. Neurosci.* **48**(8), 2795–2806 (2018).
- <sup>14</sup>J. L. Butler, P. R. Mendonça, H. P. Robinson, and O. Paulsen, "Intrinsic cornu ammonis area 1 theta-nested gamma oscillations induced by optogenetic theta frequency stimulation," *J. Neurosci.* **36**(15), 4155–4169 (2016).
- <sup>15</sup>G. Buzsáki, "Theta oscillations in the hippocampus," *Neuron* **33**(3), 325–340 (2002).
- <sup>16</sup>G. Buzsáki, *Rhythms of the Brain*, 1st ed. (Oxford University Press, New York, 2006).
- <sup>17</sup>G. Buzsáki and X.-J. Wang, "Mechanisms of gamma oscillations," *Annu. Rev. Neurosci.* **35**, 203 (2012).
- <sup>18</sup>R. T. Canolty and R. T. Knight, "The functional role of cross-frequency coupling," *Trends. Cogn. Sci.* **14**(11), 506–515 (2010).
- <sup>19</sup>R. Capocelli and L. Ricciardi, "Diffusion approximation and first passage time problem for a model neuron," *Kybernetik* **8**(6), 214–223 (1971).
- <sup>20</sup>L. L. Colgin, T. Denninger, M. Fyhn, T. Hafting, T. Bonnevie, O. Jensen, M. -B. Moser, and E. I. Moser, "Frequency of gamma oscillations routes flow of information in the hippocampus," *Nature* **462**(7271), 353 (2009).
- <sup>21</sup>S. Coombes and Á. Byrne, Next generation neural mass models. in *Nonlinear Dynamics in Computational Neuroscience*, PoliTO Springer Series, edited by F. Corinto and A. Torcini (Springer, Cham, 2019), pp. 1–16.
- <sup>22</sup>O. David and K. J. Friston, "A neural mass model for MEG/EEG: Coupling and neuronal dynamics," *NeuroImage* **20**(3), 1743–1755 (2003).
- <sup>23</sup>F. Devalle, E. Montbrío, and D. Pazó, "Dynamics of a large system of spiking neurons with synaptic delay," *Phys. Rev. E* **98**(4), 042214 (2018).
- <sup>24</sup>F. Devalle, A. Roxin, and E. Montbrío, "Firing rate equations require a spike synchrony mechanism to correctly describe fast oscillations in inhibitory networks," *PLoS Comput. Biol.* **13**(12), e1005881 (2017).
- <sup>25</sup>M. di Volo and A. Torcini, "Transition from asynchronous to oscillatory dynamics in balanced spiking networks with instantaneous synapses," *Phys. Rev. Lett.* **121**(12), 128301 (2018).
- <sup>26</sup>G. Dumont, G. B. Ermentrout, and B. Gutkin, "Macroscopic phase-resetting curves for spiking neural networks," *Phys. Rev. E* **96**(4), 042311 (2017).
- <sup>27</sup>G. B. Ermentrout and N. Kopell, "Parabolic bursting in an excitable system coupled with a slow oscillation," *SIAM J. Appl. Math.* **46**(2), 233–253 (1986).
- <sup>28</sup>D. S. Goldobin and A. V. Dolmatova, "Ott-Antonsen ansatz truncation of a circular cumulant series," *Phys. Rev. Res.* **1**(3), 033139 (2019).
- <sup>29</sup>B. Hangya, Z. Borhegyi, N. Szilágyi, T. F. Freund, and V. Varga, "GABAergic neurons of the medial septum lead the hippocampal network during theta activity," *J. Neurosci.* **29**(25), 8094–8102 (2009).
- <sup>30</sup>E. M. Holz, M. Glennon, K. Prendergast, and P. Sauseng, "Theta-gamma phase synchronization during memory matching in visual working memory," *Neuroimage* **52**(1), 326–335 (2010).
- <sup>31</sup>A. Hyafil, A.-L. Giraud, L. Fontolan, and B. Gutkin, "Neural cross-frequency coupling: Connecting architectures, mechanisms, and functions," *Trends. Neurosci.* **38**(11), 725–740 (2015).
- <sup>32</sup>S. Jahnke, R.-M. Memmesheimer, and M. Timme, "Stable irregular dynamics in complex neural networks," *Phys. Rev. Lett.* **100**, 048102 (2008).
- <sup>33</sup>B. H. Jansen and V. G. Rit, "Electroencephalogram and visual evoked potential generation in a mathematical model of coupled cortical columns," *Biol. Cybern.* **73**(4), 357–366 (1995).
- <sup>34</sup>O. Jensen and L. L. Colgin, "Cross-frequency coupling between neuronal oscillations," *Trends. Cogn. Sci.* **11**(7), 267–269 (2007).
- <sup>35</sup>J. Kaplan and J. Yorke, "Functional differential equations and approximation of fixed points," *Lecture Notes Math.* **730**, 204–227 (1979).
- <sup>36</sup>Y. Kuramoto, *Chemical Oscillations, Waves, and Turbulence* (Springer Science & Business Media, 2012), Vol 19.
- <sup>37</sup>Y. A. Kuznetsov, *Elements of Applied Bifurcation Theory* (Springer Science & Business Media, 2013), Vol. 112.
- <sup>38</sup>G. Lajoie, K. K. Lin, and E. Shea-Brown, "Chaos and reliability in balanced spiking networks with temporal drive," *Phys. Rev. E* **87**, 052901 (2013).
- <sup>39</sup>B. Lega, J. Burke, J. Jacobs, and M. J. Kahana, "Slow-theta-to-gamma phase-amplitude coupling in human hippocampus supports the formation of new episodic memories," *Cereb. Cortex* **26**(1), 268–278 (2014).
- <sup>40</sup>J. E. Lisman and O. Jensen, "The theta-gamma neural code," *Neuron* **77**(6), 1002–1016 (2013).
- <sup>41</sup>M. London, A. Roth, L. Beeren, M. Häusser, and P. E. Latham, "Sensitivity to perturbations in vivo implies high noise and suggests rate coding in cortex," *Nature* **466**, 123–127 (2010).
- <sup>42</sup>S. Luccioli and A. Politi, "Irregular collective behavior of heterogeneous neural networks," *Phys. Rev. Lett.* **105**(15), 158104+ (2010).
- <sup>43</sup>T. B. Luke, E. Barreto, and P. So, "Complete classification of the macroscopic behavior of a heterogeneous network of theta neurons," *Neural Comput.* **25**(12), 3207–3234 (2013).
- <sup>44</sup>T. B. Luke, E. Barreto, and P. So, "Macroscopic complexity from an autonomous network of networks of theta neurons," *Front. Comput. Neurosci.* **8**, 145 (2014).
- <sup>45</sup>A. Mazzoni, N. Brunel, S. Cavallari, N. K. Logothetis, and S. Panzeri, "Cortical dynamics during naturalistic sensory stimulations: Experiments and models," *J. Physiol. Paris* **105**(1-3), 2–15 (2011).
- <sup>46</sup>A. Mazzoni, S. Panzeri, N. K. Logothetis, and N. Brunel, "Encoding of naturalistic stimuli by local field potential spectra in networks of excitatory and inhibitory neurons," *PLoS Comput. Biol.* **4**(12), e1000239 (2008).
- <sup>47</sup>E. Montbrío, D. Pazó, and A. Roxin, "Macroscopic description for networks of spiking neurons," *Phys. Rev. X* **5**(2), 021028 (2015).
- <sup>48</sup>E. Ott, *Chaos in Dynamical Systems* (Cambridge University Press, 2002).
- <sup>49</sup>E. Ott and T. M. Antonsen, "Low dimensional behavior of large systems of globally coupled oscillators," *Chaos* **18**(3), 037113 (2008).
- <sup>50</sup>H. Pastoll, L. Solanka, M. C. van Rossum, and M. F. Nolan, "Feedback inhibition enables theta-nested gamma oscillations and grid firing fields," *Neuron* **77**(1), 141–154 (2013).
- <sup>51</sup>D. Pazó and E. Montbrío, "Low-dimensional dynamics of populations of pulse-coupled oscillators," *Phys. Rev. X* **4**(1), 011009 (2014).
- <sup>52</sup>A. Pikovsky, M. Zaks, M. Rosenblum, G. Osipov, and J. Kurths, "Phase synchronization of chaotic oscillations in terms of periodic orbits," *Chaos* **7**(4), 680–687 (1997).
- <sup>53</sup>I. Ratas and K. Pyragas, "Noise-induced macroscopic oscillations in a network of synaptically coupled quadratic integrate-and-fire neurons," *Phys. Rev. E* **100**(5), 052211 (2019).
- <sup>54</sup>M. Rosenblum, P. Tass, J. Kurths, J. Volkman, A. Schnitzler, and H.-J. Freund, "Detection of phase locking from noisy data, application to magnetoencephalography," in *Chaos In Brain?* (World Scientific, 2000), pp. 34–51.
- <sup>55</sup>M. P. Sceniak and M. B. MacIver, "Slow gaba mediated synaptic transmission in rat visual cortex," *BMC Neurosci.* **9**(1), 8 (2008).
- <sup>56</sup>A. Sirota, S. Montgomerly, S. Fujisawa, Y. Isomura, M. Zugaro, and G. Buzsáki, "Entrainment of neocortical neurons and gamma oscillations by the hippocampal theta rhythm," *Neuron* **60**(4), 683–697 (2008).

<sup>57</sup>P. So, T. B. Luke, and E. Barreto, "Networks of theta neurons with time-varying excitability: Macroscopic chaos, multistability, and final-state uncertainty," *Phys. D: Nonlinear Phenom.* **267**, 16–26 (2014).

<sup>58</sup>A. Treves, "Mean-field analysis of neuronal spike dynamics," *Netw. Comput. Neural Syst.* **4**(3), 259–284 (1993).

<sup>59</sup>E. Ullner and A. Politi, "Self-sustained irregular activity in an ensemble of neural oscillators," *Phys. Rev. X* **6**(1), 011015 (2016).

<sup>60</sup>F. Varela, J.-P. Lachaux, E. Rodriguez, and J. Martinerie, "The brainweb: Phase synchronization and large-scale integration," *Nat. Rev. Neurosci.* **2**(4), 229 (2001).

<sup>61</sup>J. A. White, M. I. Banks, R. A. Pearce, and N. J. Kopell, "Networks of interneurons with fast and slow  $\gamma$ -aminobutyric acid type a (GABAA) kinetics provide substrate for mixed gamma-theta rhythm," *Proc. Natl. Acad. Sci. U.S.A.* **97**(14), 8128–8133 (2000).

<sup>62</sup>M. A. Whittington and R. D. Traub, "Interneuron diversity series: Inhibitory interneurons and network oscillations *in vitro*," *Trends. Neurosci.* **26**(12), 676–682 (2003).

<sup>63</sup>H. R. Wilson and J. D. Cowan, "Excitatory and inhibitory interactions in localized populations of model neurons," *Biophys. J.* **12**(1), 1–24 (1972).